ADVANCED OPTICAL MATERIALS
www.advopticalmat.de

Chalcogenide Visible Transmissive Metasurface Optics

Hao Dai, Yilin Shi, Zezhao Ju, Kunhao Lei, Ye Luo, Jieren Song, Ruizhe Liu, Qikai Chen, Mengxue Qi, Yaoguang Ma, Lan Li,* and Hongtao Lin**

The development of innovative dielectric materials is crucial for advancing metasurface optics. Chalcogenides are well-known for their unique optical properties and broadband high transmission from visible to infrared, which promises to be an emerging material platform for metasurface optics. However, the lack of chalcogenide materials in visible transmissive metasurfaces remains. In this work, the designs and experimental works of the first chalcogenide visible transmissive metasurface optics based on the chalcogenide material $Ge_{23}Sb_7S_{70}$ (GSS) platform are presented. Taking advantage of its high refractive index and low optical loss in visible, chalcogenide metalens, focused meta-vortex, meta-holographic devices, and computational visible spectrometers are designed and fabricated with a commendable performance. This work establishes the groundwork for realizing diverse functionalities and broader integration of chalcogenide metasurfaces at visible wavelengths.

1. Introduction

Traditional optical elements control light propagation through phase accumulation generated by geometric shapes of bulk optical glasses, which has limited the miniaturization of optical elements and systems. Metasurface optics with discontinuous phase can achieve arbitrary wavefront control, which has been extensively researched and applied in many fields,[1,2] such as planar metalens,[3–5] spin-orbit manipulation,[6–8] holographic imaging,[9–11] information processing,[12,13] and biological monitoring.[14] Owing to the advantages such as small footprint, high design freedom, good compatibility with semiconductor manufacturing, and wide selection of optical materials, metasurface optics exhibit great potential to replace traditional optical elements and relatively matured diffractive optical elements. Despite the extensive use of various dielectric materials in metasurfaces across different wavelength bands, including HfO_2,[15] Nb_2O_5,[16] AlN[17] for ultraviolet band, Ta_2O_5,[18] TiO_2,[19,20] GaN,[21] SiN[22] for visible band, a-Si[23,24] and c-Si[25] for near-infrared to mid-infrared, however, the pursuit of high refractive index, broadband transparency and ease of fabrication remains essential. Therefore, the development of innovative dielectric materials is crucial for advancing metasurface optics.

Chalcogenide materials are compounds in which chalcogen elements (sulfur, selenium, tellurium, etc) are covalently combined with other elements, which are usually characterized by broadband transparency,[26–28] high refractive index,[27,29] adjustable

H. Dai, Z. Ju, K. Lei, J. Song, R. Liu, H. Lin
State Key Laboratory of Brain-Machine Intelligence
Key Laboratory of Micro-Nano Electronics and Smart System of Zhejiang Province
College of Information Science and Electronic Engineering
Zhejiang University
Hangzhou 310027, China
E-mail: hometown@zju.edu.cn

H. Dai, Z. Ju, K. Lei, J. Song, R. Liu, H. Lin
MOE Frontier Science Center for Brain Science & Brain-Machine Integration
Zhejiang University
Hangzhou 310027, China

Y. Shi, Y. Luo, L. Li
Zhejiang Key Laboratory of 3D Micro/Nano Fabrication and Characterization
Research Center for Industries of the Future
School of Engineering
Westlake University
Hangzhou 310030, China
E-mail: lilan@westlake.edu.cn

Y. Shi, Y. Luo, L. Li
Institute of Advanced Technology
Westlake Institute for Advanced Study
18 Shilongshan Road, Hangzhou 310024, China

Q. Chen, Y. Ma
College of Optical Science and Engineering
Zhejiang University
Hangzhou 310027, China
E-mail: mayaoguang@zju.edu.cn

M. Qi
Najing Science and Technology
Hangzhou 310027, China

L. Li
Westlake Institute for Optoelectronics
Fuyang, Hangzhou 311421, China

The ORCID identification number(s) for the author(s) of this article can be found under https://doi.org/10.1002/adom.202402359

DOI: 10.1002/adom.202402359

refractive index[30] and strong optical nonlinearity.[31] Some have phase-change and nonvolatile capabilities[32,33] to realize reconfigurable metasurface. Not only that, attributed to their lower boiling points, chalcogenide materials are easy to integrate and can be deposited on various substrates at low temperatures through a simple single-source thermal evaporation coating,[34] which could simplify the fabrication and expand the scenario of the metasurface. Due to these distinctive optical properties, chalcogenides are well-suited for realizing high performance and multifunctional metasurface optics.

Until now, chalcogenide metasurface has been extensively studied from infrared to terahertz. In the terahertz range, $Ge_2Sb_2Te_5$ was integrated into metasurface designs, achieving a reconfigurable broadband terahertz modulator.[28] Besides, the Huygens chalcogenide metasurface platform based on PbTe has extended the wavelength range to the mid-infrared band and realized ultra-thin mid-infrared transmissive metalenses with diffraction-limited focusing and high operating efficiency.[27] Additionally, chalcogenide topological insulators such as Bi_2Te_3 exhibit extremely high optical refractive index in the 2–10 μm infrared range, contributing to strong harmonic modulation to incident electromagnetic waves.[29] Moreover, low-loss chalcogenide material based on GeSbSeTe has been utilized in mid-infrared metasurface devices, while achieving high switch ratios for all-dielectric mid-infrared metalenses through algorithmic optimization of design.[35] Furthermore, owing to the strong nonlinearity of chalcogenide material, As_2S_3 metasurface based on a phase-locking mechanism has experimentally proved the conversion capabilities of electromagnetic waves from near-infrared to ultraviolet frequencies and exhibited minimal absorption.[31] Overall, chalcogenide materials have provided extensive capabilities and promising performance in metasurface optics from infrared to terahertz. Although chalcogenide materials excel in broadband transparency, the fabrication challenges of visible metasurface devices increase substantially as the operational wavelength decreases. Consequently, the lack of chalcogenide materials in visible transmissive metasurfaces still remains, which is a significant reason for our development of this metasurface platform. Besides its broadband transparency, the potential of chalcogenide materials, such as reconfigurability and nonlinearity, could also promote further research and application of visible metasurface.

In this work, to the best of our knowledge, we present the designs and experimental works of the first chalcogenide visible transmissive metasurface optics based on chalcogenide material $Ge_{23}Sb_7S_{70}$ (GSS) platform. Using truncated waveguide meta-units, we achieve a nearly 2π phase shift along with good nanopillar structures that closely match the original design. On this basis, we obtain three hyperboloid metalenses at different wavelengths, which could reach the diffraction limit closely, and their focusing efficiencies can reach 70–80%. Subsequently, we demonstrate focused vortex metasurfaces with various topological charges at 660 nm. Besides, utilizing the G-S algorithm method, we show chalcogenide holographic metasurfaces and achieve holographic displays at visible wavelengths. Furthermore, we design chalcogenide meta-filters and realize computational visible spectrometer by an optimization algorithm, achieving visible spectral sensing with 7 nm spectral resolution and high spectral reconstruction accuracy at 450–750 nm. In summary, the chalcogenide material we studied in this work provides a high performance metasurface platform in the visible band and promises further future research of reconfigurable and flexible metasurfaces.

2. Results and Discussion

2.1. Fabrication and Design of Chalcogenide Visible Transmissive Metasurface Platform

Visible metasurfaces have garnered significant interest due to their wide range of potential applications. **Table 1** summarizes the current state-of-the-art visible metasurface materials, all of which exhibit excellent optical properties. However, challenges such as complex deposition processes, high manufacturing costs, limited dielectric thickness, and the need for additional hard mask steps complicate the fabrication. In contrast, the GSS material presented here exhibits a high refractive index comparable to leading materials while maintaining low optical loss across the visible spectrum. A key advantage of GSS is its low-temperature thermal evaporation deposition, which allows for near-room-temperature substrate processing. This feature enables the use of GSS on various substrates, including flexible ones such as SU8 and PI,[36] thus enhancing the integration potential of our GSS metasurface platform. Moreover, GSS has a high etch rate (>5 nm $^{-1}$s) and selectivity (> 6:1), enabling the fabrication of complex metasurface structures with high aspect ratios and intricate geometries without a hard mask. These unique properties position GSS as an ideal candidate for high performance dielectric metasurfaces in the visible spectrum, offering a balance between optical performance and manufacturability.

The fabrication schematic of chalcogenide visible transmissive metasurface is illustrated in **Figure 1a**. First, the GSS film with a

Table 1. Overview of materials and processing methods for visible metasurfaces.

Material	n@visible	κ@visible	Thickness	Film preparation	Hard mask in dry etching
SiN[37]	≈2	≈0	695 nm	ICPCVD	Cr
SiO_2[38]	≈1.46	≈0	2000 nm	Fused Silica	Cr
GaN[39,40]	>2.4	≈0.01	715 nm	MBE / MOCVD	SiN / SiO_2
Ta_2O_5[18]	>2.1	≈0	400 nm	Sputtering	Al_2O_3
TiO_2[41–43]	≈2.4	<0.003	600 nm	Filling by ALD	/
TiO_2[44]	>2.1	≈0	220 nm	Evaporation	Cr
$Ge_{23}Sb_7S_{70}$	>2.3	<0.04	600 nm	Evaporation	Resist

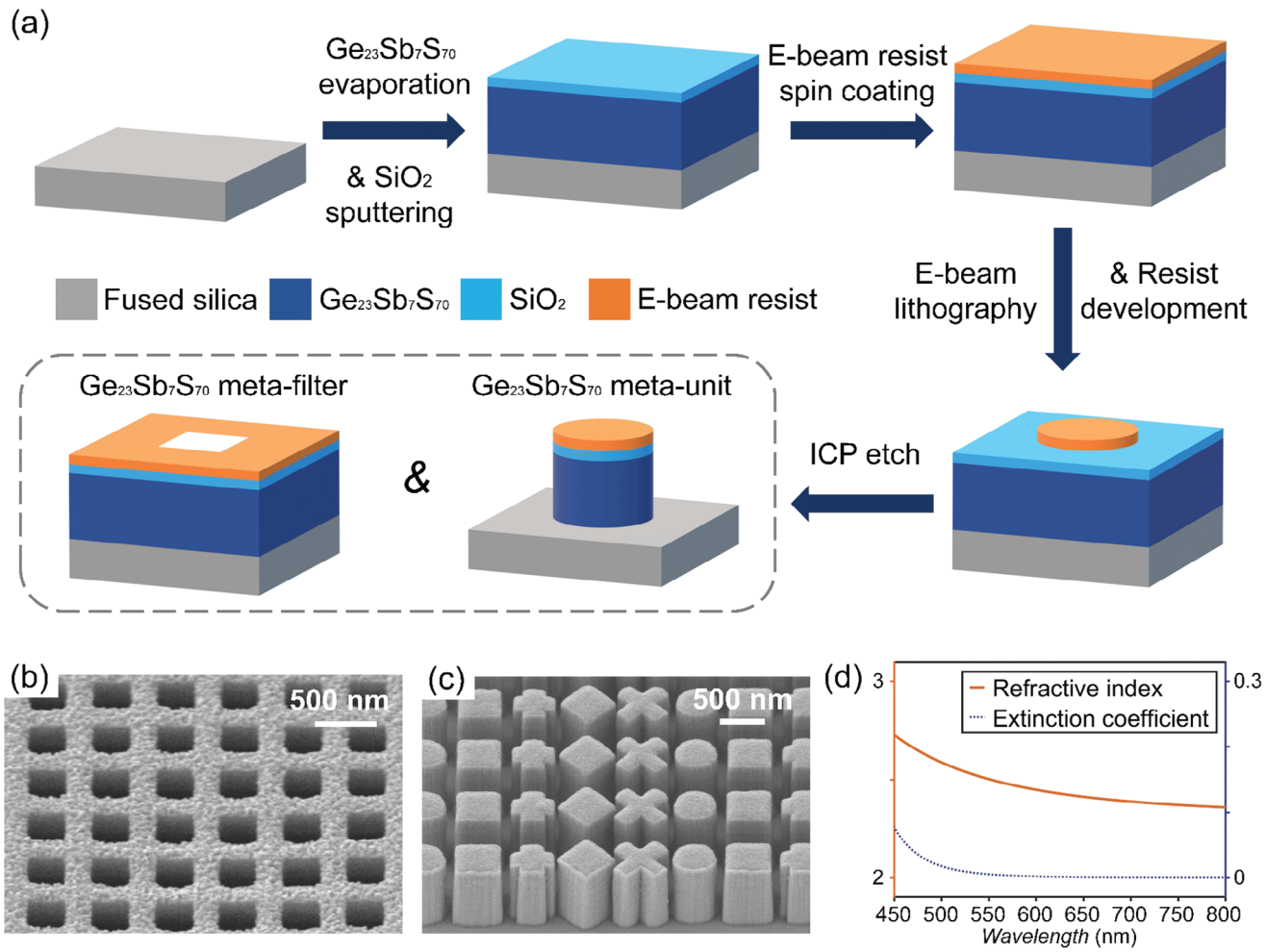

Figure 1. Development of chalcogenide visible transmissive metasurface platform. a) Fabrication process schematic of the chalcogenide metasurface platform. Chalcogenide b) nanohole meta-filters and c) nanopillar meta-units observed via scanning electron microscopy (SEM). d) Refractive index and extinction coefficient of GSS thin film deposited through thermal evaporation, acquired through ellipsometry.

thickness of ≈ 600 nm is deposited on a 700 μm thick quartz substrate by thermal evaporation with a single thermal source. The optical constants of GSS film at 450–800 nm, as shown in 1d, reveal that our prepared GSS has a relatively high optical refractive index ($n > 2.3$) and a low extinction coefficient ($\kappa < 0.04$) at visible wavelengths, serving as the principal reason for developing the chalcogenide visible metasurface platform.

Subsequently, a SiO_2 layer of ≈60 nm thick is deposited on the upper surface of the GSS film through magnetron sputtering to prevent the GSS from being corroded by the photoresist developer. After that, electron beam lithography is engaged to pattern the metasurface structures onto the photoresist. Finally, the nanoholes (Figure 1b) and nanopillars (Figure 1c) of GSS metasurface are obtained through ICP dry etching technology.

As a result of relatively high etch selectivity (> 6:1) between GSS and photoresist, the etching process can completely etch out the metasurface structures. To guarantee the GSS metasurface is completely etched, a controlled over-etching process is conducted in our fabrication, and the etching interface can still terminate at the interface between the GSS and quartz substrate. Since the protective silica layer on GSS film is thin enough, the etching and pattern-transfer process would not be affected. It merits emphasis that the photoresist and silica layer is ultimately retained in the devices to maintain the structural integrity of the metasurface devices, which are also taken into account in the optical simulations. Considering the slight increase in Ar gas flow during nanohole etching, the surfaces are subjected to more intense physical bombardment, resulting in marginally greater roughness compared to nanopillars. Nonetheless, this roughness is negligible in its effect on the performance of the meta-filters, preserving the reliability of the optical transmission matrix for computational spectrometer development.

Compared to Huygens metasurfaces, truncated waveguide metasurfaces use the propagation phase and offer greater efficiency and, unlike Pancharatnam-Berry phase metasurfaces, are not limited by the polarization of incident light, making them the preferred choice for developing transmissive metasurfaces.[45] Therefore, we use cylindrical truncated waveguide meta-units in this work, to ensure relatively high device efficiency and polarization insensitivity.

As the phase accumulation relies on phase delay in the truncated waveguide meta-units, the resulting phase shift mainly

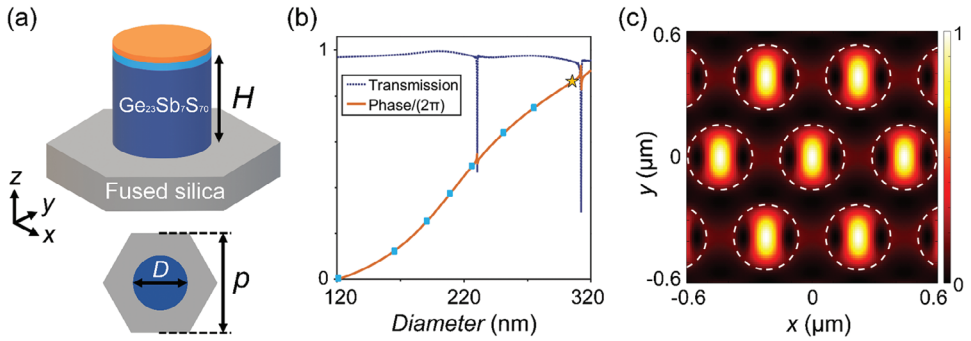

Figure 2. Design of chalcogenide meta-units. a) Schematic diagram of the hexagonal crystal lattice arrangement in the chalcogenide meta-unit and b) corresponding phase and transmission curves at 660 nm obtained from scanning diameters. c) Top views of normalized magnetic energy density at 660 nm in a periodic GSS meta-unit for diameters $D = 308.8$ nm, corresponding to the yellow star marker in (b).

correlates with the height and diameter of GSS nanopillars. Therefore, the GSS film is developed with a wavelength-level thickness of ≈600 nm to achieve approximately 2π phase shift. Besides, a subwavelength hexagonal lattice (**Figure 2a**) is utilized in the design of meta-units.[46] And the period of the meta-units is set at subwavelength scales ($p = 0.44$ μm). Figure 2b presents the simulated phase and transmission variations with changes in the diameter of hexagonally arranged GSS nanopillars at the wavelength of 660 nm, computed using 3D finite-difference time-domain simulations. Corresponding results of similar designs at 520 and 488 nm are provided in Figure S1a,b (Supporting Information). The results indicate that the phase shift of GSS meta-units in our study could cover almost 2π at visible wavelengths within a diameter range from 80 to 320 nm. To further elaborate, the top view of normalized magnetic energy density at the wavelength of 660 nm is demonstrated in Figure 2c with a diameter $D = 308.8$ nm of periodic GSS nanopillars, indicating the high concentration of the electromagnetic wave inside GSS nanopillars and thus low coupling effect between each nanopillar. These results confirm the capabilities of chalcogenide visible metasurface to enable arbitrary wavefront control while maintaining high transmission, which promises good performance of our chalcogenide visible transmissive metasurface devices.

2.2. Chalcogenide Visible Transmissive Metalens

Recently, metalenses made from visible-transparent optical materials have shown impressive performance.[4] Compared to conventional lenses and diffractive optical lenses, metalenses are lightweight, compact, semiconductor-process compatible, and most importantly, offer strong light-field manipulation capability. These characteristics confer substantial potential on them to replace traditional thick lenses. Utilizing the chalcogenide metasurface platform, here we experimentally demonstrate three GSS transmissive metalenses at visible wavelengths.

Generally, the metalens design utilizes a hyperboloid phase profile to achieve perfect focal convergence for collimated incident light,[45] finding its numerical representation in Equation (1),

$$\varphi(x, y) = \frac{2\pi}{\lambda}\left(f - \sqrt{x^2 + y^2 + f^2}\right) \quad (1)$$

Herein, (x, y) denotes the coordinates from the center of each meta-unit to the center of the device, f represents the designed focal length of metalens, and λ corresponds to the operating wavelength. Three separate GSS visible metalenses are each designed to work at respective wavelengths of 660, 520, and 488 nm. Each device has an overall size of 500 μm. The parameters for each metalens, including numerical apertures (NA) and focal lengths (f), are tailored as follows: metalens of 660 nm (Metalens 1), $NA \approx 0.15$, $f \approx 1647.8$ μm; metalens of 520 nm (Metalens 2), $NA \approx 0.13$, $f \approx 1904.6$ μm; metalens of 488 nm (Metalens 3), $NA \approx 0.12$, $f \approx 2065.8$ μm. The ideal hyperboloid phase profiles of three visible metalenses are shown in **Figures 3a**, S2ab (Supporting Information). Subsequently, the hexagonal periodic GSS meta-units are employed to develop the final GSS visible metalenses. The optical micrograph and scanning electron micrograph of the Metalens 1 are illustrated in Figure 3b,c.

To further characterize metalens performance, we have established an optical test system for metasurface optics (Figure S4a, Supporting Information). Figure 3d illustrates the normalized intensity distributions in the x-z plane of three GSS visible metalenses. These distributions are extracted from the cross-sectional profiles of the 3D optical intensity distributions, which were characterized by sequentially capturing live images in the x-y plane at 2 μm increments along the optical axis (z-axis) behind metalenses illuminated by collimated lasers. The focal positions for three metalenses were experimentally measured at respective wavelengths, resulting in focal lengths of 1658, 1910, and 2084 μm, each closely matching its design.

Additionally, the intensity distributions along the x-axis, depicted in Figure 3e, are compared with the theoretical diffraction limit defined by the ideal Airy function ($\frac{0.51 \cdot \lambda}{NA}$). The corresponding intensity distributions for each focal spot are shown in the insets of Figure 3e, with full widths at half maximum (FWHM) of 2.26, 2.08, and 2.11 μm, respectively. The experimental results demonstrate good consistency, indicating that metalenses based on the chalcogenide visible metasurface platform can achieve diffraction-limited focusing. Ultimately, the focusing efficiencies of the metalenses, defined as the ratio of the power within three times the FWHM of the focal spot to the total incident power, were experimentally measured with a 500-μm pinhole to be 80.43%, 78.11%, and 71.72% for each metalens at the corresponding wavelength (660, 520, and 488 nm). The high efficiency and optimal focal convergence performance

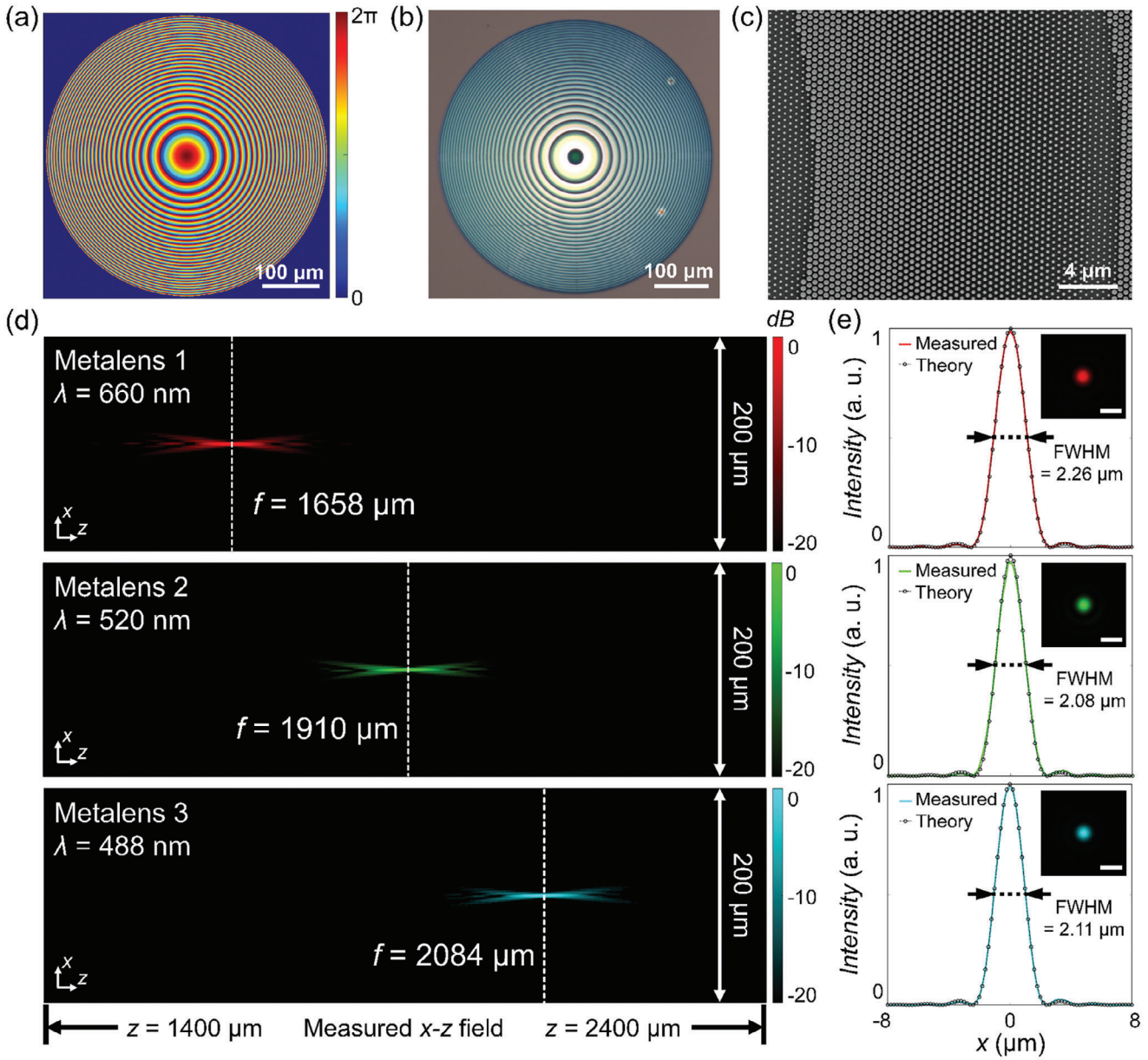

Figure 3. Design and characterization of three GSS visible metalenses. a) Ideal hyperbolic phase profiles. b) Optical micrograph and c) scanning electron micrograph of Metalens 1. d) Normalized intensity distribution in the *x*-*z* plane of three different metalenses at respective operating wavelengths (660, 520, 488 nm), with dimensions of 200 μm in the *x*-direction and 1000 μm in the *z*-direction. e) Intensity distribution along the *x*-axis of three metalenses at the corresponding focal plane (z = 1658, 1910, 2084 μm), with experimental results (colored solid lines) compared to theoretical values using the Airy function (black dots). The corresponding normalized intensity distributions at the focal plane are shown in each inset (scale bars of insets: 4 μm).

are primarily attributed to the broadband high transparency of the chalcogenide visible metasurface platform along with high-precision fabrication that aligns with the designed structures. However, the focusing efficiency reduces to 71.72% for the metalens designed at 488 nm, which is mainly due to the slightly increased optical loss of GSS at shorter wavelengths and greater manufacturing challenges, including narrower dimensional ranges and smaller structural sizes (Figure S1b, Supporting Information). These limitations could be mitigated in future work by designing more advanced geometries for the meta-units. Additionally, optimizing the composition of chalcogenide materials to reduce optical loss and enhance the refractive index in the visible spectrum represents a critical challenge and a key focus of our future research.[47,48] Nevertheless, three metalenses perform relatively high efficiency and diffraction-limited focusing, showcasing the chalcogenide metasurface platform has good capability to realize lenses at visible wavelengths, extending more support for research on wide-field, achromatic, or multifunctional metalens at visible wavelengths.

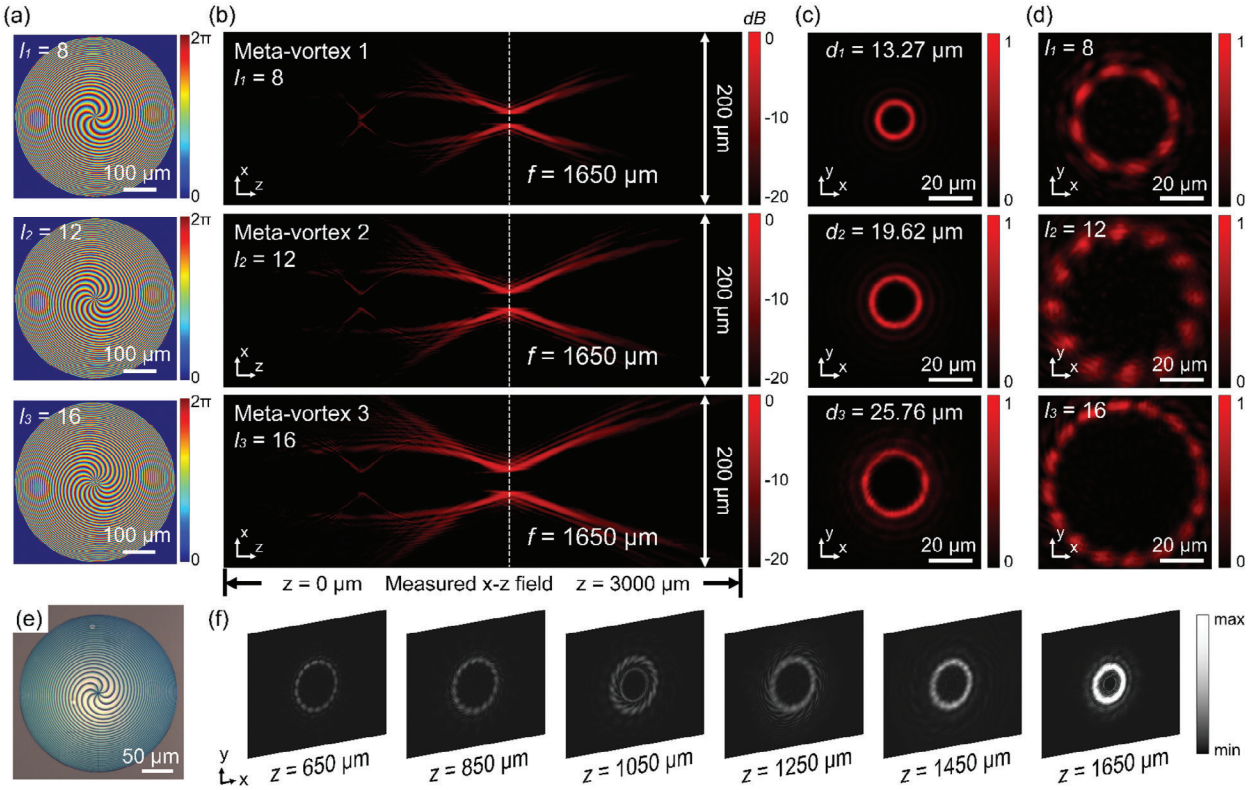

Figure 4. Design and characterization of three GSS visible meta-vortex devices. a) Ideal hyperbolic phase profiles for Meta-vortex 1, 2, and 3. b) Normalized intensity distribution in the *x*-*z* plane at 660 nm, with dimensions of 200 μm in the *x*-direction and 3000 μm in the *z*-direction. c) Normalized intensity distribution in the *x*-*y* plane with a doughnut-shaped pattern obtained at the focal plane. d) Normalized intensity distribution in the *x*-*y* plane with split fringes obtained at defocused positions. e) Optical micrograph of Meta-vortex 1 ($l = 8$). f) Intensity distribution evolution of Meta-vortex 3 ($l = 16$) in the *x*-*y* plane along the optical axis (*z*-axis).

2.3. Chalcogenide Visible Focused Meta-Vortex

Vortex beams, characterized by their helical phase and donut-shaped intensity with a dark core, effectively utilize optical orbital angular momentum (OAM) to expand communication channels. Traditional techniques such as spiral phase plates, holographic phase plates, and spatial light modulators have been employed to generate and manipulate these beams.[49] Recent advancements in metasurface optics have facilitated more compact and efficient control over optical OAM.[50] In particular, precise phase gradients in metasurfaces enhance capabilities for fine-tuning vortex beams.

In this work, we superimpose spiral phase designs on hyperboloid phase profiles used in metalens to realize the focused vortex metasurface (meta-vortex) devices with several topological charges. Employing the phase profile of the 660-nm metalens outlined above, the designed phase profile of meta-vortex devices can be numerically described by Equation (2),

$$\varphi(x, y) = \frac{2\pi}{\lambda}\left(f - \sqrt{x^2 + y^2 + f^2}\right) + l \cdot \tan^{-1}\left(\frac{y}{x}\right) \quad (2)$$

Among them, (x, y), f, λ are consistent with the definitions in Equation (1), while l represents the topological charge of the vortex beams. **Figure** 4a shows the ideal phase profiles of three focused meta-vortex devices. The sizes of these devices are all designed to be 500 μm, and the focal length f is consistently set at 1647.8 μm. The topological charges are designed with l values of 8, 12, and 16 for devices that are designated as Meta-vortex 1, Meta-vortex 2, and Meta-vortex 3, respectively. Since these devices are designed for the wavelength of 660 nm, the meta-units for layout generation can adopt the same structural parameters as depicted in Figure 2a,b. Based on the above design, the focused meta-vortex device fabricated using our chalcogenide visible metasurface platform is shown in Figure 4e, exemplified by Meta-vortex 1 with $l = 8$.

With the developed chalcogenide visible platform, we fabricated three GSS-focused meta-vortex devices at 660 nm with different orbital angular momentum and characterized them subsequently using the metasurface test system (Figure S4a, Supporting Information). Similarly, by moving the imaging system along the *z*-axis in 2 μm increments to capture live images, normalized *x*-*z* plane intensity distributions (Figure 4b) behind the focused meta-vortex devices ($z > 0$) are obtained under the illumination of the collimated 660-nm laser. It can be seen that all the focused meta-vortex devices have essentially correct and same focal length ($f = 1650$ μm). Three donut-shaped intensity distribution diagrams can be observed accurately at the focal plane (Figure 4c), corresponding to toroidal diameters of d_1, d_2, and d_3 equal to 13.27, 19.62, and 25.76 μm. The transmitted efficiencies[51,52] of

Meta-vortex 1, 2, and 3, defined as the power ratio of the generated vortex beam to the total incident power were experimentally measured to be 83.19%, 83.03%, and 82.65%, respectively. While the device efficiencies defined as the power ratio within four times the FWHM of the vortex ring to the total incident power, were measured as 77.74%, 76.34%, and 76.68% for Meta-vortex 1, 2, and 3. These results are comparable to the performance of the fabricated chalcogenide metalenses at 660 nm. The interference fringes between the surface and focal plane of meta-vortex devices are depicted in Figure 4d, which could be rendered more conspicuous by the placement of an aperture between the tube lens and the image sensor. The number of interference fringes corresponding to the generated vortex beams is completely consistent with their designed topological charges. To further elaborate, Figure 4f presents the intensity distributions of Meta-vortex 3 from z = 650 to z = 1650 μm, indicating the evolution of interference patterns for a focused vortex beam with topological charge number $l = 16$. Overall, our chalcogenide visible metasurface platform has demonstrated a good capability to generate orbital angular momentum. Additionally, its suitability for low-temperature integration on flexible substrates[36] enhances compatibility with image sensors or laser devices. These attributes highlight our platform's capabilities to realize high performance metasurface optics and enable the development of novel fully integrated photonic devices at visible bands in the future.

2.4. Chalcogenide Visible Holographic Metasurface

Computer-generated holography (CGH) generates holograms through computed phase and amplitude distributions, facilitating applications in optical encryption, 3D display, and optical detection. Conventional CGH methods, which utilize optical modulators such as spatial light modulators, are often limited by small field of view, multiple diffraction orders, and twin images due to the large pixel sizes.[53] Utilizing sub-wavelength meta-units, holographic metasurface could overcome these challenges by reducing pixel sizes. Moreover, holographic metasurface provides multidimensional control over phase, amplitude, and polarization, which could significantly enhance wavefront manipulation and improve hologram performance.[54]

In this work, we use the emblem of Zhejiang University (eagle pattern) and our team name of "ZJU CHINA GROUP" (text pattern) as the target holograms (Figures S3b, Supporting Information). The holographic phase profiles generated by the G-S iterative algorithm are presented in Figure S3c (Supporting Information), with the detailed design process described in Figure S3a (Supporting Information). Additionally, the simulated holograms at 660 nm are calculated by Fresnel diffraction theory and further compared to the target images (Figure S3d, Supporting Information). Besides, the GSS meta-units of holographic metasurface adopt square periodic cylindrical nanopillars, which can also achieve high transmission and close 2π phase coverage at 660 nm with a period of 0.44 μm (Figure S1c, Supporting Information).

Finally, we realize the holographic metasurface devices of the eagle pattern (Meta-holo 1) and text pattern (Meta-holo 2) based on the chalcogenide visible metasurface platform, with a size of about 400 μm × 400 μm and pixel counts of 910 × 910, as shown in the optical micrographs (**Figure 5**). Using the optical test system for holographic imaging (Figure S4b, Supporting Information), holograms of Meta-holo 1 (Figure 5a) and Meta-holo 2 (Figure 5b) at visible bands were observed experimentally on a white screen ≈22.5 cm from the devices. Obviously, our GSS holographic metasurfaces demonstrate clear and effective performance at visible wavelengths of 660, 520, and 488 nm, attributed to the broadband high refractive index and low loss properties of the GSS. The transmitted efficiencies of two Meta-holo devices were experimentally measured using lasers with wavelengths of 660, 520, and 488 nm. For Meta-holo 1, the transmitted efficiencies were 76.52%, 50.63%, and 41.80%, while for

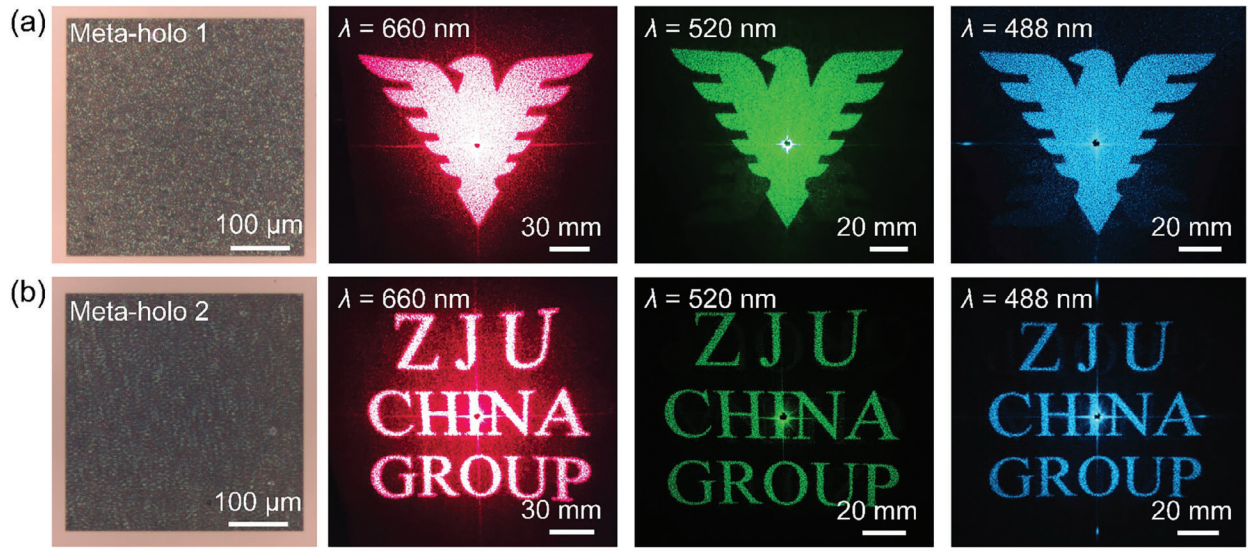

Figure 5. Characterization of GSS holographic metasurfaces. Optical micrographs and experimental holograms were obtained for a) Meta-holo 1 and b) Meta-holo 2 both at wavelengths of 660, 520, and 488 nm.

Meta-holo 2, the corresponding values were 77.35%, 50.21%, and 41.32%. It is worth noting that the two holographic phase profiles in this design are iteratively optimized only for 660 nm, leading to slight twin images and reduced efficiency at shorter visible wavelengths. Nevertheless, distinct holograms can still be observed, indicating that the chalcogenide visible metasurface platform has the potential to enable further research on color holographic imaging.

2.5. Chalcogenide Computational Visible Spectrometer

Computational spectrometers have attracted considerable attention due to their advantages in miniaturization and high integration.[55,56] Compared to miniature spectrometers utilizing narrowband filters and dispersive gratings, the computational spectrometer based on broadband filters and optimization algorithms could expand the spectral detection channels and improve the optical energy received by sensors. However, high performance metasurface filters (meta-filters) have put higher demands on broadband transmission and optical constants of optical materials. Fortunately, our proposed chalcogenide visible transmissive metasurface platform not only meets these requirements but also offers additional benefits, including ease of integration and simplified fabrication. Consequently, we utilized this platform and developed a computational spectrometer that leverages broadband spectral filtering.

Broadband spectral filters for computational spectrometers have been widely studied,[55,57] due to their impressive encoding ability. As depicted in Equation (3), an unknown incident light undergoes spectral encoding after passing through the spectral filters, resulting in the photocurrents generated on photodetectors behind the filters.

$$P(i) = \int T(i,\lambda) \cdot \eta(\lambda) \cdot I_{ph}(\lambda)\, d\lambda \tag{3}$$

Herein, $T(\lambda, i)$ represents the transmitted spectrum of each meta-filter, $I_{ph}(\lambda)$ is the spectral intensity of the incident light to be tested, $P(i)$ denotes the photocurrent received on the photodetector, and $\eta(\lambda)$ is the quantum efficiency of the photodetector. This equation can be discretized in the form of a matrix product, referring to Equation S1 and Figure S5a (Supporting Information). In this case, $T(i, \lambda)$ can be rewritten as the spectral encoding matrix $\{T_{i,\lambda_j}\}$, as well as the incident light spectrum $\{I_{\lambda_j}\}$ and current signals $\{P_i\}$. After calibrating the transmitted spectrum of each spectral filter, the incident light spectrum $I_{ph}(\lambda)$ can thus be reconstructed by solving linear equations with optimization algorithms. For broadband spectral encoding in computational spectral reconstruction, the complexity and linear independence of the encoding transmission matrix are particularly crucial for achieving high spectral resolution.[58] Traditional optical filters, such as those based on dyes or multilayer thin films, lack the ability to provide the necessary complexity and linear independence. In contrast, chalcogenide visible meta-filters can generate abundant and narrower peaks and valleys in the transmission spectrum while maintaining high broadband transmittance. This effect significantly enhances the spectral resolution of the computational spectrometer. The favorable etching properties of GSS enable the design of meta-filters with more complex structures through advanced simulations and inverse design methods, which could further enhance the resolution by achieving more intricate spectral responses.

In this research, we combine the chalcogenide visible transmissive metasurface platform with optimization algorithms and realize a computational visible spectrometer based on the GSS meta-filters. To optimize the spectral encoding performance of meta-filters, we conduct simulation designs of various shapes of periodic GSS nanoholes. Then, a library of spectral responses is obtained by scanning the geometric parameters of meta-filters. To enhance the encoding performance of the meta-filters, we first evaluate and preprocess their transmitted spectra by removing those with overly broad or narrow peaks or valleys. While narrower peaks and valleys can improve spectral resolution, we must also consider the trade-off with the sampling accuracy of our calibration equipment. Therefore, we exclude structures where the peaks or valleys exceed the resolution limit of the monochromator. Subsequently, utilizing a genetic algorithm, we selected 400 sets of meta-filter parameters with the highest non-correlation (Figure S5b and Table S1, Supporting Information). Following the fabrication process of the chalcogenide metasurface platform mentioned above, we realized GSS meta-filters operating at 450–750 nm with a total dimension of 1 mm and individual meta-filter dimension of 40 µm (**Figure 6a**).

To calibrate the spectral transmission of the GSS meta-filters, we used a visible monochromator source in the optical test system (Figure S4a, Supporting Information). Figure 6b describes the spectral transmission curves and schematic structures of two typical meta-filters (hexagonal periodic circle nanohole and square periodic square nanohole), while the complete calibrated transmission of 400 meta-filters is provided in Figure S5c (Supporting Information). These meta-filters are combined with a visible monochrome CMOS image sensor, resulting in a computational visible spectrometer at 450–750 nm. To solve Equation S1 (Supporting Information) and improve the robustness of the final results, we introduce a regularization term (Equation S2, Supporting Information) and gradient optimization algorithms to realize the spectral reconstruction.

Figure 6c illustrates the reconstruction results for a series of narrowband single-peak spectral signals at 450–750 nm with FWHM of ≈5 nm, achieving spectral accuracy with mean squared error (MSE) < 0.03% and central wavelength error <0.5 nm. Subsequently, we demonstrate the spectral resolution capability of a computational spectrometer for dual-peak spectra (both FWHM ≈ 5 nm) with gradually approaching central wavelengths, as shown in Figure 6d. It can be observed that our spectrometer exhibits a spectral resolution of ≈7 nm for the narrowband dual-peak spectra. Furthermore, the reconstruction capability of our spectrometer for broad spectral signals is also characterized. A commercial RGB light panel with a digitally adjustable color ratio is used to generate broad visible spectra. For varying RGB ratios, as shown in Figure 6e, the reconstruction results for the broad visible spectra are essentially consistent with commercial spectrometers, ultimately achieving spectral accuracy with MSE < 0.8%. The foregoing discussions highlight that the GSS meta-filters have good capability for spectral sensing at visible wavelengths, revealing the considerable potential of the

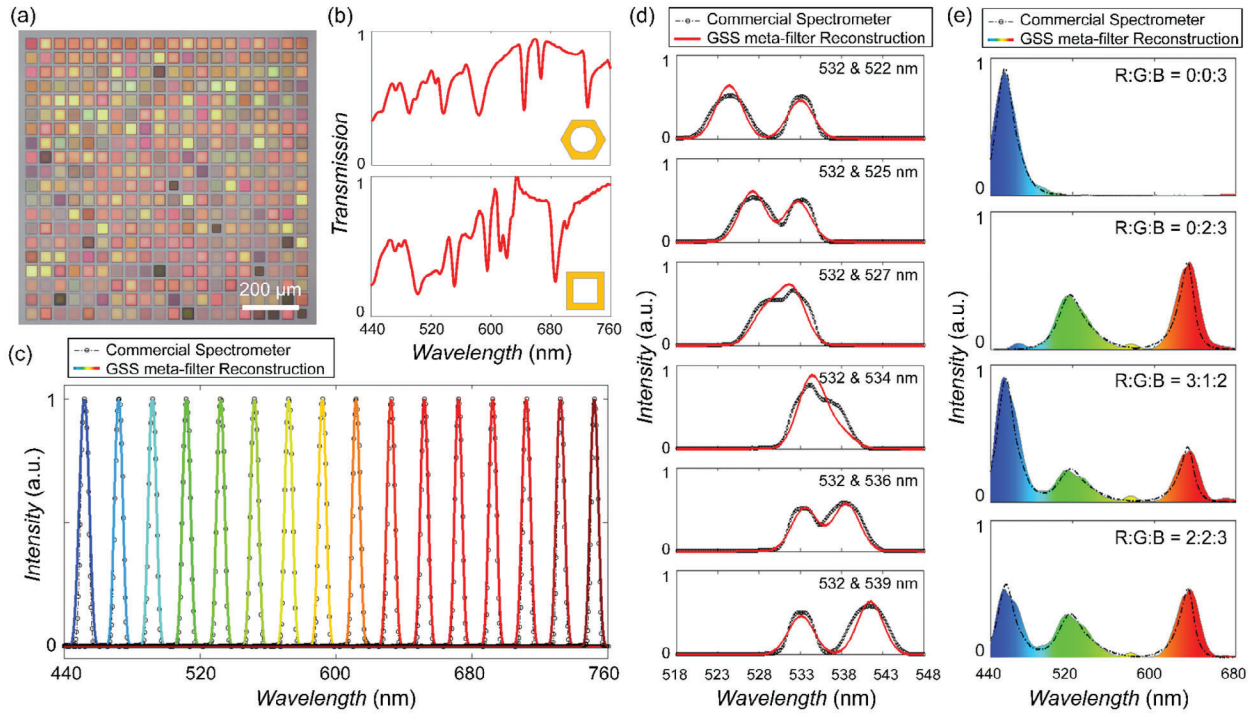

Figure 6. Design and characterization of computational visible spectrometer based on GSS meta-filters. a) Optical micrograph of the fabricated GSS meta-filters array. b) Structure schematic of two meta-filters with corresponding experimental measured transmission spectra. c) Spectral reconstruction of 300 single-peaked lights at wavelengths of 450–750 nm (colored curves). d) Spectral reconstruction results (red curves) corresponding to a series of dual-peak spectra combining a 532 nm spectral line from a narrowband filter with FWHM of ≈5 nm and a single-peak spectral generated by a tunable monochromator. e) Spectral reconstruction results correspond to broad spectra produced by a commercial RGB light panel (color-filled). The black dashed line represents the spectra measured by a commercial spectrometer, serving as the reference for the spectral reconstruction results.

chalcogenide visible transmissive metasurface platform for visible spectral engineering.

3. Conclusion

In summary, we innovatively developed a chalcogenide visible metasurface platform utilizing GSS material. GSS exhibits a high optical refractive index ($n > 2.3$) and low optical loss ($\kappa < 0.04$) at visible wavelengths. Besides, it can be easily deposited on various substrates through a simple low-temperature thermal evaporation process. Additionally, the high etching selectivity (>6:1) in ICP dry etching enables the fabrication of high-quality chalcogenide visible metasurface devices. Subsequently, we experimentally demonstrated metalenses operating at 660 nm, 520 nm, and 488 nm, achieving near-diffraction-limit focusing with focusing efficiencies of 80.43%, 78.11%, and 71.72%, respectively. By incorporating the spiral phase, we designed meta-vortex devices characterized by topological charges $l = 8$, 12, and 16. Observations at the focal plane and defocused positions confirm the results consistent with the designed distribution of angular momentum. Besides, the two holographic metasurface devices exhibit satisfactory holographic imaging performance across the visible bands, despite being designed specifically for wavelengths of 660 nm. Finally, utilizing nanohole-based meta-filters, we fabricated a computational visible spectrometer operating at 450–750 nm. The spectrometer performed reconstruction accuracy > 99.97% and central wavelength error < 0.5 nm for narrowband single-peak spectra, spectral resolution of ≈7 nm for narrowband dual-peak spectra, and spectral accuracy > 99.2% for broad RGB spectra.

It is noteworthy that although these GSS metasurface devices are based on typical metasurface designs, they already exhibit impressive device performance. This work expands the material system for visible metasurface optics and provides new prospects for broader integration and diverse designs of metasurface in the future, including the development of multifunctional and high performance metasurface devices through machine learning and topological optimization. Considering the capabilities of easy integration and phase change possessed by chalcogenide materials, our research establishes an essential foundation for the advancement of flexible metasurfaces and phase-change chalcogenide metasurfaces at visible wavelengths.

4. Experimental Section

The experimental details, including fabrication, characterization, simulation, and measurement, are listed in the Supporting Information.

Supporting Information

Supporting Information is available from the Wiley Online Library or from the author.

Acknowledgements

H.D. and Y.L.S. contributed equally to this work. This work was supported by the National Natural Science Foundation of China (92150302, 62175202, 12104375, 62222511), the Zhejiang Provincial Natural Science Foundation of China (LD22F040002, LR22F050006), Open Fund of the State Key Laboratory of Integrated Optoelectronics (IOSKL2020KF05), the Fundamental Research Funds for the Central Universities (2021QNA5007), the State Key Laboratory of Advanced Optical Communication Systems and Networks (2022GZKF005), the Key Project of Westlake Institute for Optoelectronics (Grant No. 2024GD002), the Research Center for Industries of the Future (RCIF) at Westlake University (210230006022302/002) and the STI 2030–Major Projects grant (2021ZD0200401 (Y.M.)). The authors thank ZJU Micro-Nano Fabrication Center, State Key Laboratory of Chemical Engineering at Zhejiang University, Westlake Center for Micro/Nano Fabrication and Instrumentation, and Service Center for Physical Sciences at Westlake University, Najing Science and Technology Ltd. for the facility support. The authors thank Xue Wang for the ebeam lithography process.The authors thank Liming Shan for the film deposition.

Conflict of Interest

The authors declare no conflict of interest.

Data Availability Statement

The data that support the findings of this study are available from the corresponding author upon reasonable request.

Keywords

chalcogenide glass, hologram, metalens, OAM, spectrometer

Received: September 1, 2024
Revised: February 2, 2025
Published online: February 17, 2025

[1] N. Yu, P. Genevet, M. A. Kats, F. Aieta, J.-P. Tetienne, F. Capasso, Z. Gaburro, *Science* **2011**, *334*, 333.
[2] N. Yu, F. Capasso, *Nat. Mater.* **2014**, *13*, 139.
[3] M. Khorasaninejad, W. T. Chen, R. C. Devlin, J. Oh, A. Y. Zhu, F. Capasso, *Science* **2016**, *352*, 1190.
[4] M. Khorasaninejad, F. Capasso, *Science* **2017**, *358*, eaam8100.
[5] W. T. Chen, A. Y. Zhu, F. Capasso, *Nat. Rev. Mater.* **2020**, *5*, 604.
[6] H. Sroor, Y.-W. Huang, B. Sephton, D. Naidoo, A. Vallés, V. Ginis, C.-W. Qiu, A. Ambrosio, F. Capasso, A. Forbes, *Nat. Photonics* **2020**, *14*, 498.
[7] M. Liu, P. Huo, W. Zhu, C. Zhang, S. Zhang, M. Song, S. Zhang, Q. Zhou, L. Chen, H. J. Lezec, A. Agrawal, Y. Lu, T. Xu, *Nat. Commun.* **2021**, *12*, 2230.
[8] L. Gong, Q. Zhao, H. Zhang, X.-Y. Hu, K. Huang, J.-M. Yang, Y.-M. Li, *Light Sci. Appl.* **2019**, *8*, 27.
[9] G. Zheng, H. Mühlenbernd, M. Kenney, G. Li, T. Zentgraf, S. Zhang, *Nat. Nanotechnol.* **2015**, *10*, 308.
[10] Z.-L. Deng, M. Jin, X. Ye, S. Wang, T. Shi, J. Deng, N. Mao, Y. Cao, B.-O. Guan, A. Alù, G. Li, X. Li, *Adv. Funct. Mater.* **2020**, *30*, 1910610.
[11] B. Xiong, Y. Liu, Y. Xu, L. Deng, C.-W. Chen, J.-N. Wang, R. Peng, Y. Lai, Y. Liu, M. Wang, *Science* **2023**, *379*, 294.
[12] Y. Zhou, H. Zheng, I. I. Kravchenko, J. Valentine, *Nat. Photonics* **2020**, *14*, 316.
[13] S. Wang, L. Li, S. Wen, R. Liang, Y. Liu, F. Zhao, Y. Yang, *Nano Lett.* **2023**, *24*, 356.
[14] X. Chen, T. Wu, Z. Gong, J. Guo, X. Liu, Y. Zhang, Y. Li, P. Ferraro, B. Li, *Light Sci. Appl.* **2021**, *10*, 242.
[15] C. Zhang, S. Divitt, Q. Fan, W. Zhu, A. Agrawal, Y. Lu, T. Xu, H. J. Lezec, *Light Sci. Appl.* **2020**, *9*, 55.
[16] K. Huang, J. Deng, H. S. Leong, S. L. K. Yap, R. B. Yang, J. Teng, H. Liu, *Laser Photonics Rev.* **2019**, *13*, 1800289.
[17] Z. Hu, L. Long, R. Wan, C. Zhang, L. Zhang, J. Yan, H. Duan, L. Wang, *Opt. Lett.* **2020**, *45*, 3466.
[18] C. Zhang, L. Chen, Z. Lin, J. Song, D. Wang, M. Li, O. Koksal, Z. Wang, G. Spektor, D. Carlson, H. J. Lezec, W. Zhu, S. Papp, A. Agrawal, *Light Sci. Appl.* **2024**, *13*, 23.
[19] M. Khorasaninejad, A. Y. Zhu, C. Roques-Carmes, W. T. Chen, J. Oh, I. Mishra, R. C. Devlin, F. Capasso, *Nano Lett.* **2016**, *16*, 7229.
[20] L. Yu, Y. Fan, Y. Wang, C. Zhang, W. Yang, Q. Song, S. Xiao, *Laser Photonics Rev.* **2020**, *14*, 1900324.
[21] S. Wang, P. C. Wu, V.-C. Su, Y.-C. Lai, M.-K. Chen, H. Y. Kuo, B. H. Chen, Y. H. Chen, T.-T. Huang, J.-H. Wang, R.-M. Lin, C.-H. Kuan, T. Li, Z. Wang, S. Zhu, D. P. Tsai, *Nat. Nanotechnol.* **2018**, *13*, 227.
[22] Z.-B. Fan, Z.-K. Shao, M.-Y. Xie, X.-N. Pang, W.-S. Ruan, F.-L. Zhao, Y.-J. Chen, S.-Y. Yu, J.-W. Dong, *Phys. Rev. Appl.* **2018**, *10*, 014005.
[23] A. Arbabi, Y. Horie, A. J. Ball, M. Bagheri, A. Faraon, *Nat. Commun.* **2015**, *6*, 7069.
[24] Y. Shi, H. Dai, R. Tang, Z. Chen, Y. Si, H. Ma, M. Wei, Y. Luo, X. Li, Q. Zhao, Y. Ye, J. Jian, C. Sun, K. Bao, Y. Ma, H. Lin, L. Li, *Nanophotonics* **2023**, *13*, 1339.
[25] K. Ou, F. Yu, G. Li, W. Wang, J. Chen, A. E. Miroshnichenko, L. Huang, T. Li, Z. Li, X. Chen, W. Lu, *Laser Photonics Rev.* **2021**, *15*, 2100020.
[26] S. G.-C. Carrillo, L. Trimby, Y.-Y. Au, V. K. Nagareddy, G. Rodriguez-Hernandez, P. Hosseini, C. Ríos, H. Bhaskaran, C. D. Wright, *Adv. Opt. Mater.* **2019**, *7*, 1801782.
[27] L. Zhang, J. Ding, H. Zheng, S. An, H. Lin, B. Zheng, Q. Du, G. Yin, J. Michon, Y. Zhang, Z. Fang, M. Y. Shalaginov, L. Deng, T. Gu, H. Zhang, J. Hu, *Nat. Commun.* **2018**, *9*, 1481.
[28] S. Zhang, X. Chen, K. Liu, H. Li, Y. Xu, X. Jiang, Y. Xu, Q. Wang, T. Cao, Z. Tian, *PhotoniX* **2022**, *3*, 7.
[29] H. N. S. Krishnamoorthy, G. Adamo, J. Yin, V. Savinov, N. I. Zheludev, C. Soci, *Nat. Commun.* **2020**, *11*, 1692.
[30] Y. Zhang, J. B. Chou, J. Li, H. Li, Q. Du, A. Yadav, S. Zhou, M. Y. Shalaginov, Z. Fang, H. Zhong, C. Roberts, P. Robinson, B. Bohlin, C. Ríos, H. Lin, M. Kang, T. Gu, J. Warner, V. Liberman, K. Richardson, J. Hu, *Nat. Commun.* **2019**, *10*, 4279.
[31] J. Gao, M. A. Vincenti, J. Frantz, A. Clabeau, X. Qiao, L. Feng, M. Scalora, N. M. Litchinitser, *Nat. Commun.* **2021**, *12*, 5833.
[32] P. Hosseini, C. D. Wright, H. Bhaskaran, *Nature* **2014**, *511*, 206.
[33] X. Yin, M. Schäferling, A.-K. U. Michel, A. Tittl, M. Wuttig, T. Taubner, H. Giessen, *Nano Lett.* **2015**, *15*, 4255.
[34] H. Lin, Y. Song, Y. Huang, D. Kita, S. Deckoff-Jones, K. Wang, L. Li, J. Li, H. Zheng, Z. Luo, H. Wang, S. Novak, A. Yadav, C.-C. Huang, R.-J. Shiue, D. Englund, T. Gu, D. Hewak, K. Richardson, J. Kong, J. Hu, *Nat. Photonics* **2017**, *11*, 798.
[35] M. Y. Shalaginov, S. An, Y. Zhang, F. Yang, P. Su, V. Liberman, J. B. Chou, C. M. Roberts, M. Kang, C. Rios, Q. Du, C. Fowler, A. Agarwal, K. A. Richardson, C. Rivero-Baleine, H. Zhang, J. Hu, T. Gu, *Nat. Commun.* **2021**, *12*, 1225.
[36] Y. Luo, C. Sun, H. Ma, M. Wei, J. Li, J. Jian, C. Zhong, Z. Chen, R. Tang, K. A. Richardson, H. Lin, L. Li, *Opt. Express* **2022**, *30*, 26534.
[37] Z.-B. Fan, Z.-K. Shao, M.-Y. Xie, X.-N. Pang, W.-S. Ruan, F.-L. Zhao, Y.-J. Chen, S.-Y. Yu, J.-W. Dong, *Phys. Rev. Appl.* **2018**, *10*, 014005.

[38] J.-S. Park, S. Zhang, A. She, W. T. Chen, P. Lin, K. M. A. Yousef, J.-X. Cheng, F. Capasso, *Nano Lett.* **2019**, *19*, 8673.
[39] G. Brière, P. Ni, S. Héron, S. Chenot, S. Vézian, V. Brändli, B. Damilano, J.-Y. Duboz, M. Iwanaga, P. Genevet, *Adv. Opt. Mater.* **2019**, *7*, 1801271.
[40] B. H. Chen, P. C. Wu, V.-C. Su, Y.-C. Lai, C. H. Chu, I. C. Lee, J.-W. Chen, Y. H. Chen, Y.-C. Lan, C.-H. Kuan, D. P. Tsai, *Nano Lett.* **2017**, *17*, 6345.
[41] P. Huo, C. Zhang, W. Zhu, M. Liu, S. Zhang, S. Zhang, L. Chen, H. J. Lezec, A. Agrawal, Y. Lu, T. Xu, *Nano Lett.* **2020**, *20*, 2791.
[42] M. Khorasaninejad, W. T. Chen, R. C. Devlin, J. Oh, A. Y. Zhu, F. Capasso, *Science* **2016**, *352*, 1190.
[43] R. C. Devlin, M. Khorasaninejad, W. T. Chen, J. Oh, F. Capasso, *Proc. Natl. Acad. Sci.* **2016**, *113*, 10473.
[44] Y. Chen, H. Deng, X. Sha, W. Chen, R. Wang, Y.-H. Chen, D. Wu, J. Chu, Y. S. Kivshar, S. Xiao, C.-W. Qiu, *Nature* **2023**, *613*, 474.
[45] H.-T. Chen, A. J. Taylor, N. Yu, *Rep. Prog. Phys.* **2016**, *79*, 076401.
[46] C. Chen, X. Xiao, X. Ye, J. Sun, J. Ji, R. Yu, W. Song, S. Zhu, T. Li, *Light Sci. Appl.* **2023**, *12*, 288.
[47] R. Woods-Robinson, Y. Han, H. Zhang, T. Ablekim, I. Khan, K. A. Persson, A. Zakutayev, *Chem. Rev.* **2020**, *120*, 4007.
[48] *J. Non-Cryst. Solids* **2003**, *330*, 1.
[49] L. Stoyanov, S. Topuzoski, G. G. Paulus, A. Dreischuh, *Eur. Phys. J. Plus* **2023**, *138*, 702.
[50] H. Ahmed, H. Kim, Y. Zhang, Y. Intaravanne, J. Jang, J. Rho, S. Chen, X. Chen, *Nanophotonics* **2022**, *11*, 941.
[51] K. Zhang, Y. Yuan, D. Zhang, X. Ding, B. Ratni, S. N. Burokur, M. Lu, K. Tang, Q. Wu, *Opt. Express* **2018**, *26*, 1351.
[52] C. Zhou, W.-B. Lee, S. Gao, H. Li, C.-S. Park, D.-Y. Choi, S.-S. Lee, *Laser Photonics Rev.* **2021**, *15*, 2000581.
[53] H. Gao, X. Fan, W. Xiong, M. Hong, *Opto-Electron. Adv.* **2021**, *4*, 210030.
[54] Q. Song, X. Liu, C.-W. Qiu, P. Genevet, *Appl. Phys. Rev.* **2022**, *9*, 011311.
[55] Z. Wang, S. Yi, A. Chen, M. Zhou, T. S. Luk, A. James, J. Nogan, W. Ross, G. Joe, A. Shahsafi, K. X. Wang, M. A. Kats, Z. Yu, *Nat. Commun.* **2019**, *10*, 1020.
[56] J. Xiong, X. Cai, K. Cui, Y. Huang, J. Yang, H. Zhu, W. Li, B. Hong, S. Rao, Z. Zheng, S. Xu, Y. He, F. Liu, X. Feng, W. Zhang, *Optica* **2022**, *9*, 461.
[57] H. Song, Y. Ma, Y. Han, W. Shen, W. Zhang, Y. Li, X. Liu, Y. Peng, X. Hao, *Adv. Theory Simul.* **2021**, *4*, 2000299.
[58] J. Oliver, W.-B. Lee, H.-N. Lee, *Opt. Express* **2013**, *21*, 3969.

